JACS
JOURNAL OF THE AMERICAN CHEMICAL SOCIETY
Article
pubs.acs.org/JACS

Mechanism of the Reduction of the Native Intermediate in the Multicopper Oxidases: Insights into Rapid Intramolecular Electron Transfer in Turnover

David E. Heppner, Christian H. Kjaergaard, and Edward I. Solomon*

Department of Chemistry, Stanford University, 333 Campus Drive, Stanford, California 94305-5080, United States

Supporting Information

ABSTRACT: The multicopper oxidases (MCOs) are the family of enzymes that catalyze the 4-electron reduction of O_2 to H_2O coupled to the four 1-electron oxidations of substrate. In the catalytic cycle electrons are transferred intramolecularly over ~13 Å from a Type 1 (T1) Cu site that accepts electrons from substrate to a trinuclear Cu cluster (TNC) where O_2 is reduced to H_2O at rapid rates consistent with turnover (560 s^{-1}). The oxygen reduction mechanism for the MCOs is well-characterized, whereas the rereduction is less understood. Our initial study of *Rhus vernicifera* Laccase (Heppner et al. *J. Am. Chem. Soc.* **2013**, *135*, 12212) experimentally established that the native intermediate (NI), the species formed upon O−O bond cleavage, is reduced with an IET rate >700 s^{-1} and is the catalytically relevant fully oxidized form of the enzyme, rather than the resting state. In this report, we present kinetic and spectroscopic results coupled to DFT calculations that evaluate the mechanism of the 3 e^-/3 H^+ reduction of NI, where all three catalytically relevant intramolecular electron transfer (IET) steps are rapid and involve three different structural changes. These three rapid IET processes reflect the sophisticated mechanistic control of the TNC to enable rapid turnover. All three IET processes are fast due to the associated protonation of the bridging oxo and hydroxo ligands, generated by O−O cleavage, to form water products that are extruded from the TNC upon full reduction, thereby defining a unifying mechanism for oxygen reduction and rapid IET by the TNC in the catalytic cycle of the MCOs.

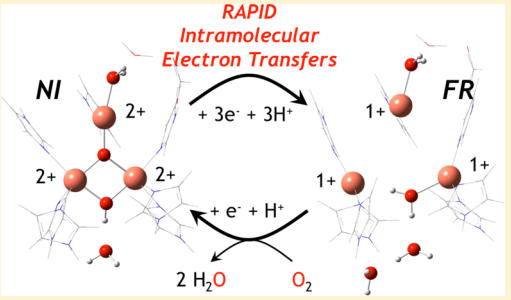

INTRODUCTION

The reduction of dioxygen (O_2) to water is performed in nature by the multicopper oxidases (MCOs) in order to carry out a variety of single-electron oxidations of metal ion or organic substrates.[1−3] These enzymes have been of particular interest in a number of areas including their relevance to human health (ceruloplasmin),[4] bioremediation (laccases),[5] and application as oxidation catalysts in biofuel cells (laccases and bilirubin oxidases).[6,7]

The MCOs require at least four Cu's to accomplish their activity: a type 1 (T1)[8−10] Cu site and a trinuclear Cu (TNC)[11,12] site, that in the resting state is composed of a mononuclear type 2 (T2) and antiferromagnetically coupled binuclear type 3 (T3) Cu centers (Figure 1). The T1 site is solvent accessible and receives electrons from substrate. This T1 center then transfers the electrons through the protein via a conserved Cys-His pathway over ~13 Å to the TNC, which is buried in the protein, where O_2 binds and is reduced. The coppers of the TNC in the oxidized resting state are ligated by 8 histidines in conserved His-X-His motifs where three each ligate the T3 coppers and two ligate the T2. The T2 is additionally coordinated by an aquo-derived hydroxide while the T3s are bridged by a μ_2-hydroxide (μ_2-OH) providing a superexchange pathway for the antiferromagnetic coupling of the T3 Cu(II)'s.[13] Two conserved carboxylate residues are located near the TNC in all MCOs: D94 (numbered from the Fet3p sequence),[14] hydrogen bonded to the T2 hydroxo ligand and near the T3b, functions as an essential negative charge. Also, there is E487 at the bottom of the TNC near the T3s, which is the source of protons for the O_2 reduction at the TNC.[15−18]

The mechanism of O_2 reduction by the MCOs has been well-characterized and occurs in two 2-electron steps (Figure 2).[2] First, the fully reduced (FR) state reacts with O_2 at a rate of 1.7 × 10^6 M^{-1} s^{-1} to form a peroxy intermediate (Figure 2).[19] In this intermediate, O_2 is reduced by 2 electrons and is coordinated by all three Cu's of the TNC, where the T2 and T3b Cu's are oxidized, being closest to the negative D94 that lowers their redox potentials.[17] With an electron transferred from the T1 and a proton from E487, the O−O bond is cleaved to give the native intermediate (NI), where all Cu's are oxidized and the oxygen atoms originating from O_2 are fully reduced and bound as a μ_3-oxo in the center of the cluster and a μ_2-OH bridging the T3s (Figure 2).[20] Reoxidation rates of *Rhus vernicifera* Laccase have determined a lower-limit rate for O−O bond cleavage of >350 s^{-1} from stopped-flow kinetics (Figure 2) and of *Trametes versicolor* Laccase a lower-limit rate of >25 000 s^{-1} has been determined from microsecond freeze-hyper quench studies.[21] These kinetic measurements imply

Received: September 4, 2014
Published: November 19, 2014

   dx.doi.org/10.1021/ja509150j | J. Am. Chem. Soc. 2014, 136, 17788−17801

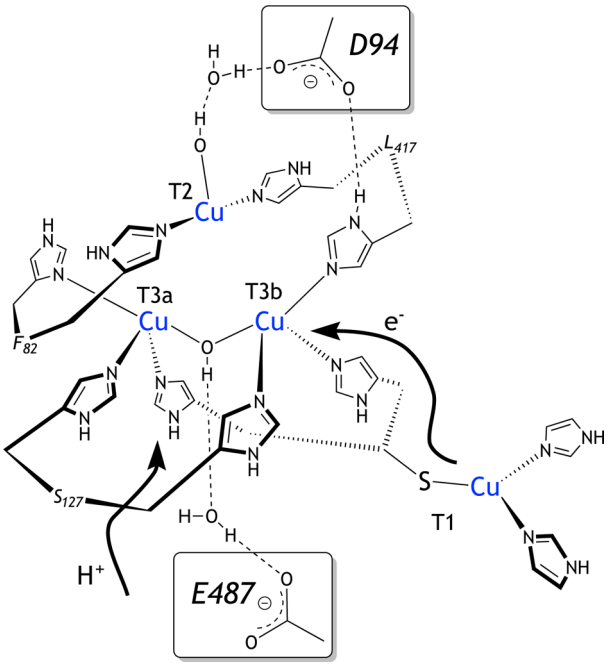

Figure 1. Structure of the trinuclear cluster of the fully oxidized (4 Cu^{II}) resting state of the multicopper oxidases including essential second-sphere carboxylate residues. Arrows indicate the flow of electrons and protons from the T1 Cu and E487, respectively. Residue numbers are for Fet3p.

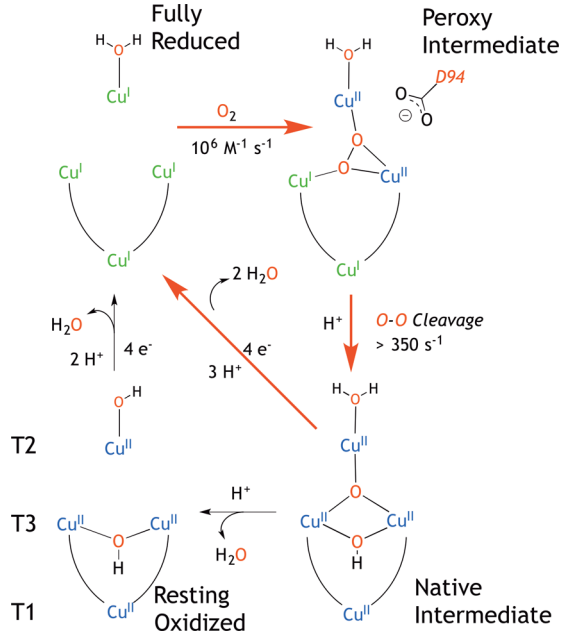

Figure 2. Mechanism of the multicopper oxidases.

rapid IET from the T1 to the TNC in O_2 reduction. The triangular topology of the TNC enables rapid O−O bond cleavage with a low barrier in the second 2-electron step making this overall process an effective 4-electron reduction of O_2.[17] After the O−O bond has been cleaved, NI decays slowly (0.058 s^{-1} at 23 °C) in the absence of substrate to the resting oxidized form.[22] Alternatively, in the presence of substrate, NI is reduced directly to the fully reduced form.[23]

While much is known about the O_2 reduction mechanism in the MCOs, less is understood concerning the half of the catalytic cycle where substrate is oxidized and the TNC is reduced. In this case, four electrons must reduce the enzyme with three undergoing intramolecular transfer over 13 Å from the T1 to the TNC. Considerable insight into the mechanism of the MCOs has been derived from studies on the Japanese Tree Laccase (Lc) from *Rhus vernicifera*, which exhibits fast turnover (k_{cat} = 560 s^{-1}).[24] For a long time, the mechanism of the reduction of the enzyme in catalysis went undefined since intramolcular electron transfer (IET) rates from the T1 to the TNC in the resting oxidized form were measured to be far slower (k^{IET} = 1.1 s^{-1})[25] than turnover (k_{cat} = 560 s^{-1}).[24] Alternatively, it had been proposed that IET rates in the reduction of NI could be fast and therefore catalytically relevant.[1,2] We have recently experimentally determined that this is the case and shown that NI, not the fully oxidized resting enzyme, as is studied in crystallography,[26,27] is the catalytically relevant fully oxidized form capable of rapid IET (k^{IET}_1 > 700 s^{-1}) consistent with turnover (k_{cat} = 560 s^{-1}).[23] This significant rate enhancement (>10^3) for IET in NI relative to the resting TNC was determined to be due to the large driving force for proton-coupled electron transfer (PCET) caused by the strong basicity of the μ_3-oxo of NI. Subsequently, fast IET rates (~460 s^{-1}) were reported in turnover conditions of a small laccase from *S. coelicolor* with single molecule measurements consistent with our findings establishing rapid IET rates in the catalytic cycle.[28] However, our understanding to this point only focuses on the first IET step in the reduction of NI; two additional rapid IET steps are required to fully reduce NI and complete the catalytic cycle.

In this report, we extend our initial study on *Rhus vernicifera* Laccase to now characterize the molecular mechanism of the 3 e^-/3 H^+ processes in the reduction of NI in the catalytic cycle of the MCOs. The reduction of NI is examined via kinetic modeling of stopped-flow (SF) absorption data correlated to freeze-quench electron paramagnetic resonance (FQ-EPR) measurements to determine intermediates formed in this process. These data are coupled to density functional theory (DFT) calculations of these electron and proton transfer processes to fully characterize the molecular mechanism of all three rapid IET steps in NI reduction that enable fast turnover in the MCOs.

RESULTS AND ANALYSIS

Kinetics. The reduction of NI was monitored by spectral changes in stopped-flow (SF) absorption. The reaction of fully reduced Lc with equal molar O_2 shows initial rapid (~10^6 M^{-1} s^{-1}) formation of NI based on the appearance of the 365 nm band due to the μ_3-oxo to Cu^{II}_3 charge transfer (CT) at the TNC and the 614 nm S_{cys} to Cu^{II} CT of the oxidized T1 site.[19,23,29] With excess hydroquinone (H_2Q) reductant present, NI is reduced as monitored by the loss of the 365 nm band of the TNC (Figure 3A, red) with the first electron into the TNC in a [H_2Q] dependent process (182 M^{-1} s^{-1}). Since this TNC absorption band is eliminated after the first IET from the T1, a lower limit rate for the first IET step of >700 s^{-1} was obtained.[23]

The 614 nm band, which reflects the concentration of the oxidized T1 site present, decays in a multiphasic fashion where at early time points (within 20 s; Figure 3A) the T1 initially remains mostly oxidized, and then more rapidly decays to the fully reduced enzyme. The decay rate of this band increases with [H_2Q] (Figure 3B). At high H_2Q concentrations (>500-electron equivalent excess), the T1 is reduced on the same time

dx.doi.org/10.1021/ja509150j | J. Am. Chem. Soc. 2014, 136, 17788−17801

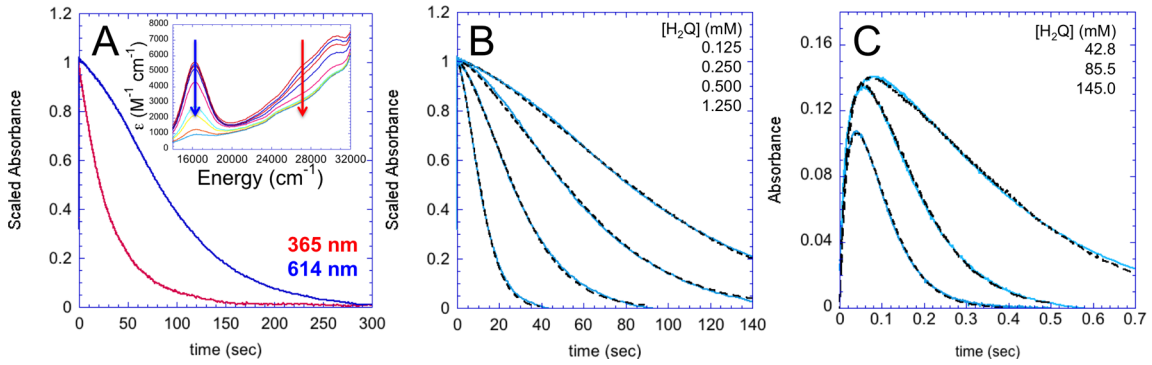

Figure 3. Stopped-flow absorption traces of the reduction of NI. [Lc] = [O_2] = 50 μM at pH 7.5 and 4 °C. (A) Scaled absorption traces of the T1 (614 nm, blue) and TNC (365 nm, red) charge transfer bands in the reduction of NI with 0.125 mM H_2Q excess. Inset: absorption spectra from 1 to 300 s. (B) Scaled absorption traces (solid light blue) and fits (dashed black) of the 614 nm band with 0.125, 0.250, 0.500, and 1.250 mM [H_2Q] excess. (C) Traces (solid light blue) and fits (dashed black) of the 614 nm band with 42.8, 85.5, and 145.0 mM [H_2Q] excess. Part A reprinted with permission from ref 23. Copyright 2013 American Chemical Society.

scale that it is needed in the O_2 reaction to form NI (Figure 3C). The kinetics monitored by the T1 reduction reflects the entire 4-electron process in the reduction of NI since the T1 Cu mediates all three IET steps. Therefore, modeling the trace of the 614 nm band provides an experimental probe of the second and third IET steps.

In the 4-electron reduction of NI, each incoming electron enters the enzyme via the reduction of the T1 Cu followed by transfer through the protein to the TNC (Figure 1). This proceeds via a seven step, 4-electron mechanism (Scheme 1).

Scheme 1. Model of the Full 4-Electron Mechanism of the Reduction of the MCOs

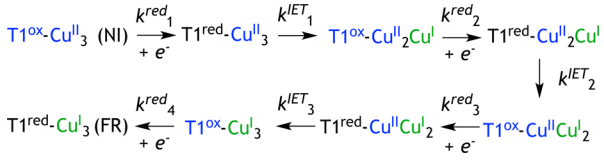

The redox states are denoted with the superscript "ox" or "red" for the T1 and by the oxidation states of the Cu's of the TNC. The rates governing this process are the [H_2Q] dependent T1 reduction rate (k^{red}) and the [H_2Q] independent IET rates (k^{IET}) from the T1 to the TNC. Starting with the formation of NI, this sequence of T1 reduction followed by IET occurs three times to fully reduce the TNC, and the fourth electron reduces the T1 giving the fully reduced state. Since the 614 nm band is proportional to the concentration of the oxidized T1, all species with $T1^{ox}$ will contribute to the trace (i.e., intensity) of this band.

The model in Scheme 1 was initially fit to the 614 nm decay kinetics with 50 electron-equivalents (1.25 mM) excess H_2Q to ensure pseudo-first-order behavior for the T1 reduction steps. The rates for the first T1 reduction (k^{red}_1 = 0.207 s^{-1}) and first IET rate ($k^{IET}_1 \geq 700$ s^{-1}), where rates slower than this lower limit cause the fit to deviate from the data, were determined from the 365 nm decay in the same experiment and fixed in the fitting of the 614 nm reduction kinetics. The first fit to the data (fit A; Figure 4A) has all four k^{red} rates in Scheme 1 equal to the first T1 reduction rate ($k^{red}_{1,2,3,4}$ = 0.207 s^{-1}), with the first IET rate set equal to 700 s^{-1}, and the second and third IET rates were modeled as fast (>2 s^{-1} under these conditions). This fit shows a T1 intensity reduction that is too slow and is inconsistent with the data (dashed black line compared to the data in blue in Figure 4A). In fit B (Figure 4B), the second, third, and fourth T1 reduction rates are increased to approximately twice k^{red}_1 with the same IET rates as in fit A. This leads to faster 614 nm decay, but fails to capture the curvature of the trace, in particular at early times (0–5 s in Figure 4B). To properly model the absorbance at early time, fit C (Figure 4C) includes reversibility at the second IET step with $K_{eq}^{IET}{}_2 = k^{IET}{}_{+2}/k^{IET}{}_{-2} \approx 1$. Including this equilibrium with the same rates as in fit A correctly fits the absorbance decay at early time points, but the overall decay is too slow. In fit D (Figure 4D), the second, third, and fourth T1 reduction rates in fit C are increased as in fit B. This fit properly models the data and represents the minimal model required to describe the time dependence of the 614 nm absorption decrease. This shows that NI is reduced in a mechanism where the three T1 reduction rates are twice as fast as the first, and importantly, the second IET step is reversible implying a low driving force for this process.

This minimal model (Figure 4D) can be expanded to further probe the kinetics of the third IET step, since this step is contained within the kinetics of the 614 nm band and precedes the fourth and final reduction of the T1. First considering the data with 50 electron equivalent excess in Figure 5A, modeling an equilibrium constant for the third IET step shows that it must be irreversible ($K_{eq}^{IET}{}_3 > 1$). Additionally, fitting IET rates with the 614 nm data at higher H_2Q (Figure 5B) affords a lower limit for $k^{IET}{}_3 > 500$ s^{-1}.

Applictaion of this model to the entire data set (Figure 3B,C), with $k^{IET}{}_1$ = 700 s^{-1}, $K_{eq}^{IET}{}_2$ = 1.0, and $k^{IET}{}_3$ = 500 s^{-1} and the T1 reduction rates varying proportionally to the concentration of H_2Q, reveals a global fit to the kinetics of the 614 nm band (Table 1). The second order rates of the T1 reduction steps are obtained from the linear dependence of these rates across the entire data set where k^{red}_1 = 150 M^{-1} s^{-1} is in accord with the rate observed from loss of the 365 nm band of NI.[23] Additionally, this model is consistent with H_2Q as the only reductant for all four T1 reduction steps in the reduction of NI. Since the T1 is a single electron acceptor, a semiquinone (SQ) would be produced that could reduce the T1 with an approximately 3 orders of magnitude faster rate than H_2Q ($k(H_2Q) \approx 10^2$ M^{-1} s^{-1}; $k(SQ) \approx 10^5$ M^{-1} s^{-1}) based on its 350 mV lower reduction potential.[30,31] However, the rate of disproportionation of SQ is 10^7–10^8 M^{-1} s^{-1}

dx.doi.org/10.1021/ja509150j | J. Am. Chem. Soc. 2014, 136, 17788–17801

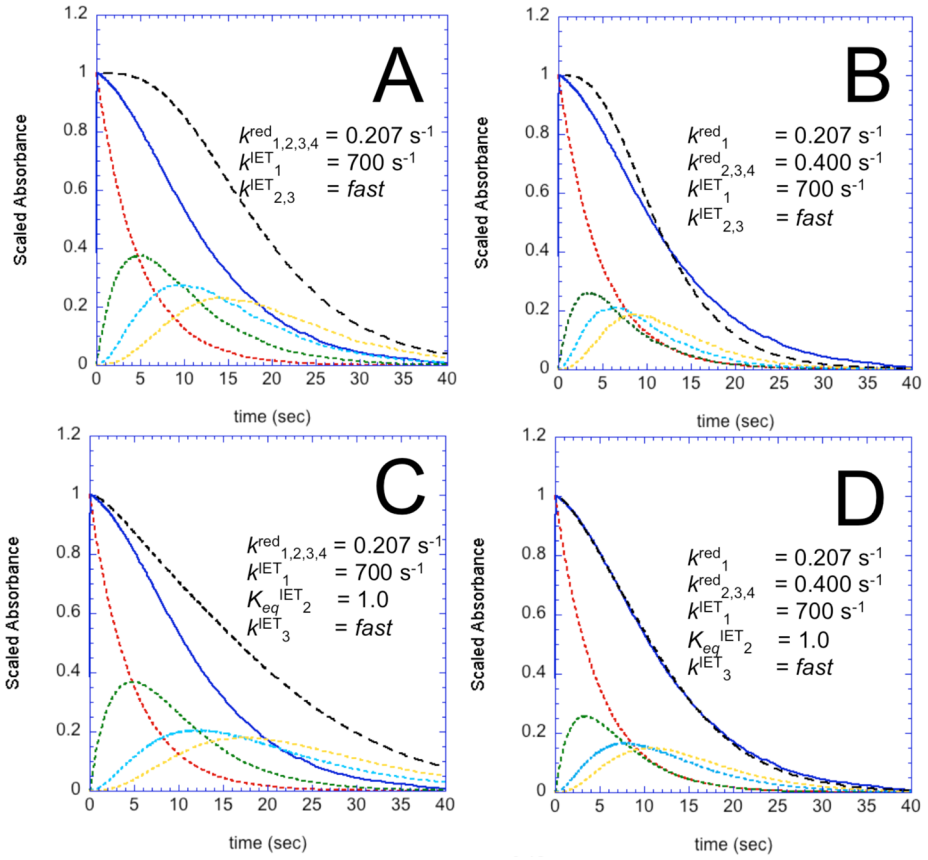

Figure 4. Kinetic fits to the scaled 614 nm absorbance decay with [Lc] = [O_2] = 50 μM and [H_2Q] = 1.25 mM at pH 7.5 and 4 °C. Each fit (A–D) showing the experimental scaled absorbance of 614 nm (dark blue solid), speciation of the intermediates: $T1^{ox}$-Cu^{II}_3 (red dotted), $T1^{ox}$-$Cu^{II}_2Cu^{I}$ (green dotted), $T1^{ox}$-$Cu^{II}_1Cu^{I}_2$ (light blue dotted), $T1^{ox}$-Cu^{I}_3 (gold dotted), and summation these species (dashed black).

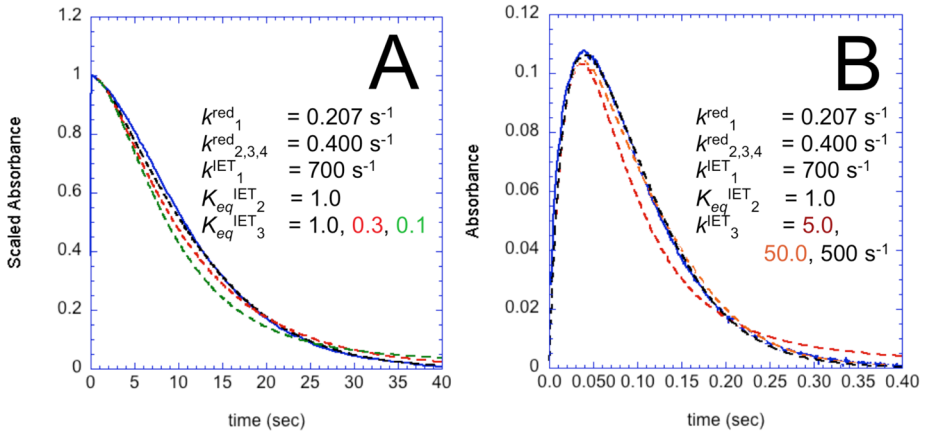

Figure 5. Fits of the 614 nm absorption traces to probe the third IET step [Lc] = [O_2] = 50 μM at pH 7.5 and 4 °C. (A) 1.25 mM H_2Q data fit with equilibrium constants of 1.0, 0.3, and 0.1 (dashed lines in black, red, and green, respectively) for the third step. (B) 145.0 mM H_2Q with k^{IET}_3 = 5, 50, and 500 s^{-1} (red, orange, and black, respectively).

Table 1. Kinetic Parameters in the Global Fit of the 614 nm Absorbance in the Reduction of NI Corresponding to the Mechanism in Scheme 1

k^{red}_{1}	150 M^{-1} s^{-1}
k^{red}_{2}, k^{red}_{3}, k^{red}_{4}	350 M^{-1} s^{-1}
k^{IET}_{1}	>700 s^{-1}
$K_{eq}{}^{IET}_{2}$	1.0
k^{IET}_{3}	>500 s^{-1}

implying that all SQ formed will disproportionate before reducing the T1.[32] This is consistent with early kinetic studies on the reduction of *Rhus vernicifera* Laccase by H_2Q where no significant SQ involvement was observed.[33] The kinetic data at high H_2Q concentrations (Figure 3C) contain an additional rate of 1.2 × 10^6 M^{-1} s^{-1} for the formation of NI, consistent with a previous estimate in the absence of reductant.[19]

This model reveals a number of key findings about the mechanism of the reduction of NI. First, the T1 reduction rate increases for the last three steps. This is consistent with our

dx.doi.org/10.1021/ja509150j | J. Am. Chem. Soc. 2014, 136, 17788–17801

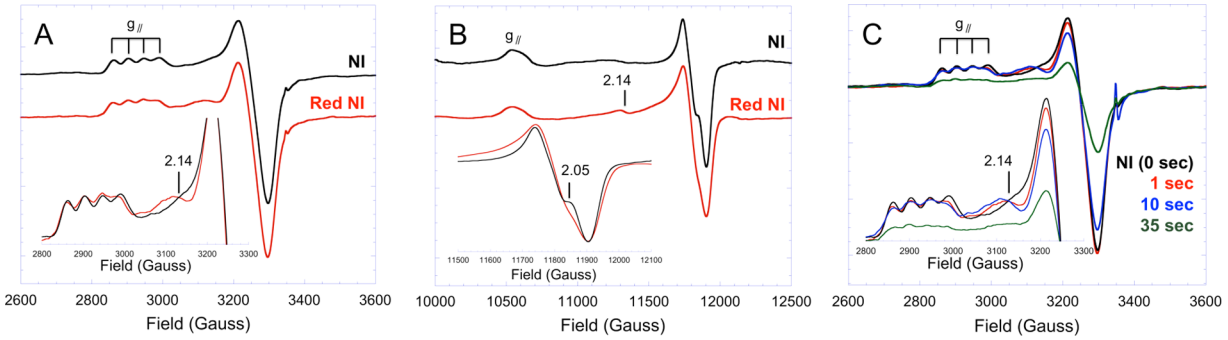

Figure 6. FQ-EPR spectra of NI (black) and NI reduced (Red NI; red) with 5 electron equivalents of H_2Q at pH = 7.5. (A) X-band spectra. Inset: overlay showing additional derivative signal at g = 2.14. (B) Q-band spectra. Inset: overlay of the $g_\perp$ region showing additional intensity at g = 2.05. (C) Time dependence of the FQ-EPR spectra in the reduction of NI. X-band FQ-EPR spectra of NI (black, 0 s) and 5 electron equivalent reduced NI at different times [1 s (red), 10 s (blue), and 35 s (green)] reacted at 4 °C.

earlier spectroscopic findings that the structure and redox state of the TNC affect the structure of the T1 center.[34] Second, the curvature at early time points of the 614 nm trace requires that the second IET is reversible with a $K_{eq}{}^{IET}{}_2 \approx 1$, and therefore, this process occurs with a low driving force. The fits in this model are not sensitive to the actual rates for the forward and reverse processes, but this IET step must be rapid ($k^{IET}{}_2 \geq 560$ s^{-1}) to be consistent with turnover and the IET rates from catalytic single molecule measurments.[24,28] Lastly, the third IET step is irreversible and has a lower limit rate of $k^{IET}{}_3 > 500$ s^{-1} consistent with this step having a large driving force. Taken together with the previous findings, where the first IET step also has a large driving force,[23] the kinetics of all three rapid IET steps are revealed. Importantly, these IET steps exhibit different kinetic behavior; namely, the second IET has a lower driving force than the first and third. Since these IET steps are all rapid in turnover, there must be a mechanistic difference between at least the second IET step relative to the first and third.

Spectroscopy. Freeze-quench electron paramagnetic resonance (FQ-EPR) data were obtained to correlate to the kinetics and define potential paramagnetic intermediates in NI reduction. NI is trapped by reacting fully reduced Lc with O_2 quenched after 1 s.[29] The 77 K X-band FQ-EPR spectrum of NI exhibits the typical signal of the oxidized T1 site with $g_{\|}$ = 2.30 and $A_{\|}$ = |47| × 10^{-4} cm^{-1} (Figure 6A, black), where contributions from the 3 coupled Cu(II)'s of the TNC in NI are not observed at temperatures >20 K.[29] FQ-EPR samples of reduced NI (Red NI in Figure 6, red) were obtained by reacting fully reduced Lc with O_2 but in the presence of 5 electron-equivalents of H_2Q to reduce NI in parallel with the SF experiments. The 77 K X-band EPR spectrum of this reaction quenched after 1 s is composed mostly of the signal of the oxidized T1 but exhibits an additional signal at g = 2.14 (Figure 6A, red). The overlay of the X-band FQ-EPR spectra of NI and Red NI show this extra signal has a derivative shape using the signal of the T1 of NI as a reference (Figure 6A, expanded). A similar 77 K X-band FQ-EPR signal was observed by Reinhammar upon reacting Lc reduced with excess electron equivalents of H_2Q with O_2.[35] This g = 2.14 signal is also observed in FQ-EPR samples at 77 K in Q-band (Figure 6B). An overlay of the Q-band spectra in the $g_\perp$ region (~11500 − 12000 G) of NI and Red NI shows an additional signal intensity contribution in the Red NI FQ-EPR spectrum at g = 2.05 (Figure 6B, expanded). No other contribution from this new species is evident in the X-band or Q-band EPR spectra. From these data, an additional EPR detectable species is present in the reduction of NI exhibiting a derivative signal centered at g = 2.14 and potentially another negative feature at g = 2.05.

FQ-EPR samples at different reaction times at 4 °C show the time course of the reduction of NI (Figure 6C). The starting point (0 s) is defined by the 77 K X-band EPR spectrum of NI (Figure 6C, black). When NI is reduced, the derivative feature at g = 2.14 clearly increases at early times (0 to 1 and 10 s in Figure 6C, expanded black to red to blue). As the reaction proceeds to 35 s (Figure 6C, green), the FQ-EPR intensity of both the T1 and the g = 2.14 signals decreases. These data show that as the T1 reduces in NI reduction, the g = 2.14 derivative signal first grows in and then decays along with the T1. Attempts to quantify the time dependence of the intermediate EPR signal are difficult due to large errors in spin-quantifying its contribution to the total EPR intensity (see Supporting Information Figure S4). Since this signal is observed at 77 K, this new signal reflects an $S = {}^1/_2$ EPR active intermediate, a 1-electron hole ($Cu^{II}Cu^{I}{}_2$) form of the TNC generated by the reduction of NI. A geometric perturbation of the T1 can be ruled out since the absorption spectra from stopped-flow show no changes to the T1 region over the course of the reduction of NI (Figure 3A, inset). This signal will be correlated to possible structures obtained from DFT calculations below.

DFT Calculations on Proton-Coupled Electron Transfer to the TNC of NI. Expanding on experimental insights from the kinetic model and FQ-EPR data, DFT calculations were performed to understand, on a molecular level, the nature of the three IET processes in the reduction of NI. The active site model of NI contains the histidines ligated to the Cu's, the D94 carboxylate near the T2 and T3b Cu's, which has been shown to provide an essential negative charge,[15,17] and a water hydrogen bonded to the hydroxo ligand that bridges the T3 Cu's, which is observed in the resting crystal structures (Figure 7; PDB: 1GYC).[27] To distinguish different reduced and protonated structures, the optimized structures will be denoted with $\mathbf{NI}^{xe,yH}$ where x and y denote the number of electrons and protons transferred to NI, respectively. The free energies of reduction are computed with respect to a reduced and oxidized T1 model and free energies of protonation from solvent are computed using the solvation free energy of the proton.[36] In order to understand the factors that tune rapid IET, the calculated free energies and inner-sphere reorganization energies are correlated with Marcus Theory where rates of

dx.doi.org/10.1021/ja509150j | J. Am. Chem. Soc. 2014, 136, 17788−17801

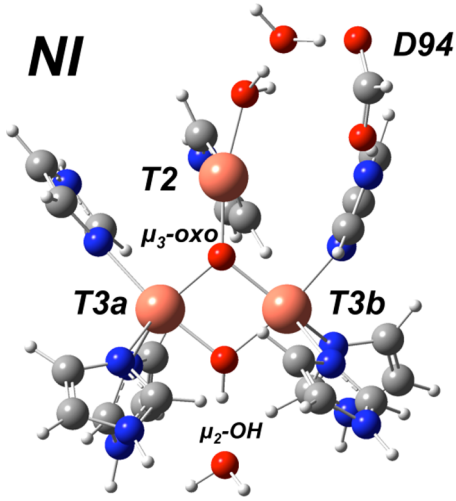

Figure 7. Geometry optimized structure of NI determined from spectroscopy. Histidine on the T2 omitted for clarity. Colors: Cu, orange; O, red; N, blue; C, gray; H, white.

IET are dependent on the thermodynamic driving force ($\Delta G°$), reorganization energy (λ), which contains the energy to reorganize solvent (outer-sphere; λ_o) and bonds (inner-sphere; λ_i) upon redox of the donor and acceptor, and the electronic coupling between the donor and acceptor (H_{DA}).[37] In comparing the IET steps, differences in reorganization energy are assumed to mostly reflect the changes of the inner-sphere of the TNC as the inner-sphere reorganization of the T1, and all the outer-sphere reorganization energies should be similar for each IET step. Also, H_{DA} is assumed to be the same since the ET pathway is identical for each IET step.

Since reducing NI involves protons and electrons, mechanisms of proton-coupled electron transfer (PCET) must be considered.[38,39] These processes can occur in a stepwise manner where electron transfer (ET) occurs prior to proton transfer (PT), denoted "ET/PT" or in the opposite order "PT/ET". The electron and proton can transfer in a concerted process, denoted "EPT". The inner-sphere reorganization energies for the concerted EPT processes (λ_i^{EPT}) were estimated using a method employed by Hammes-Schiffer and co-workers (see Methods section).[40,41]

First IET Step. The first IET to **NI** has been shown to be a concerted EPT process, which explains the $>10^3$ rate enhancement over IET to the resting TNC (Figure 8, Table 2).[23] The first electron into NI reduces the T3a Cu, as seen from spin densities of $\mathbf{NI^e}$ in Table 2. The T3a Cu of the TNC is furthest from D94 and therefore has a higher redox potential than the T3b and T2 Cu's.[17] This reduction results in the

Table 2. Selected Distances and Cu Spin Densities of the Structures of the First IET Step

	NI	NI^e	NI^H (T3W)	NI^H	$NI^{e,H}$
Distances (Å)					
T3a–T3b	2.982	3.328	3.259	3.325	3.718
T3a–T2	3.474	3.427	3.480	3.642	4.219
T3b–T2	3.463	3.288	3.397	3.934	3.719
T3a–O(μ_3-oxo)[a]	1.920	1.982	1.868	2.058	
T3b–O(μ_3-oxo)[a]	1.978	1.918	1.978	2.428	1.984
T2–O(μ_3-oxo)[a]	1.881	1.914	2.018	1.934	1.867
T3a–O(μ_2-OH)[b]	1.929	3.149		1.946	2.101
T3b–O(μ_2OH)[b]	1.898	1.906	2.053	1.892	1.919
T2–OH_2	2.025	2.107	2.015	1.953	1.959
Cu Spin Densities					
T3a	0.66	−0.03	0.57	0.68	0.03
T3b	0.62	0.58	0.64	0.69	0.61
T2	−0.56	−0.51	0.61	−0.62	−0.60

[a]O(μ_2-OH) in $\mathbf{NI^H}$, $\mathbf{NI^{e,H}}$. [b]O(-OH_2) in $\mathbf{NI^H}$ (T3W).

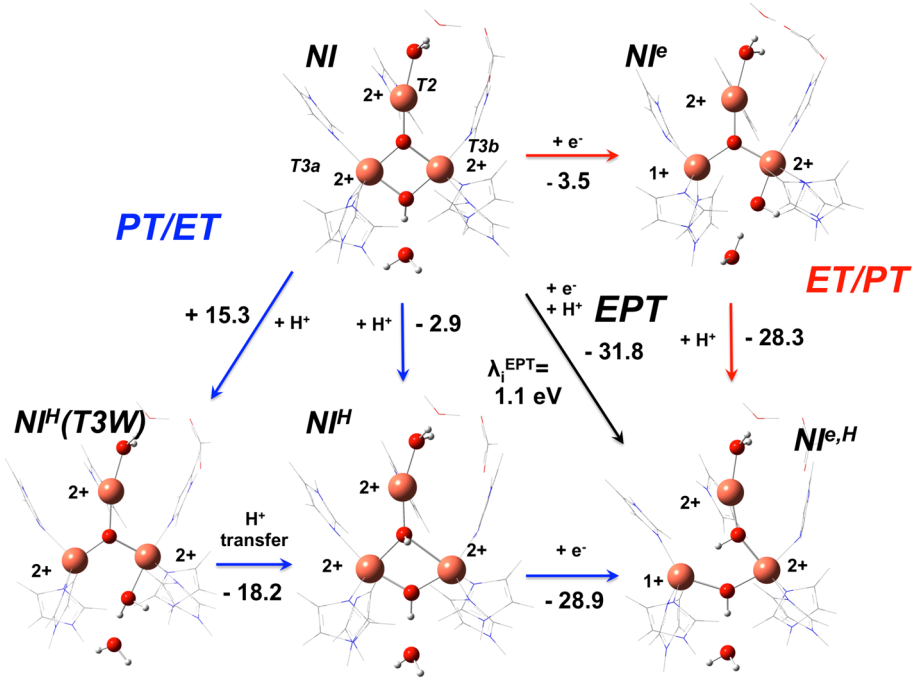

Figure 8. DFT calculations of the first IET step. All energies reflect Gibbs free energies (ΔG) in units of kcal/mol. Distances and spin densities for these structures are reported in Table 2. Histidine of the T2 removed for clarity. Colors: Cu, orange; O, red; N, blue; C, gray; H, white. ET/PT, PT/ET, and EPT pathways labeled in red, blue, and black, respectively.

dx.doi.org/10.1021/ja509150j | J. Am. Chem. Soc. 2014, 136, 17788−17801

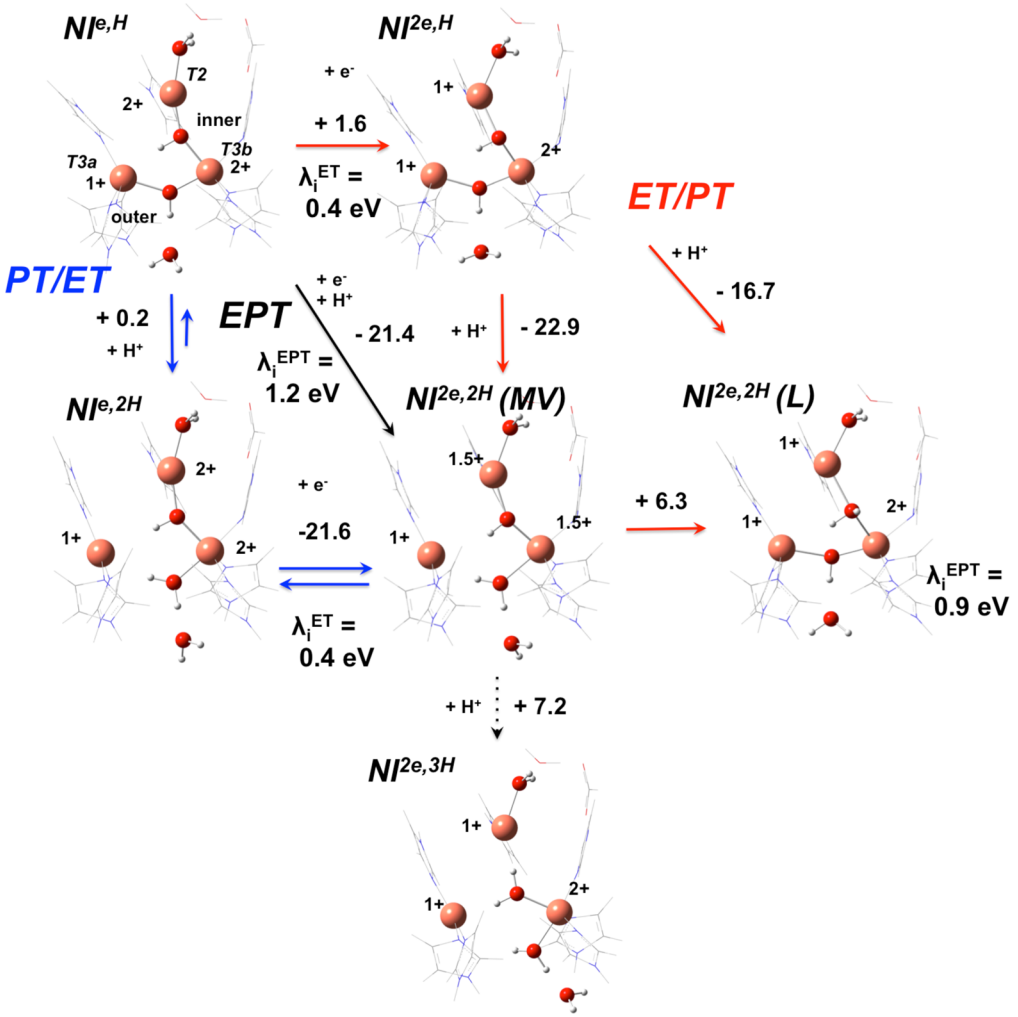

Figure 9. DFT calculations of the second IET step. All energies reflect Gibbs free energies (ΔG) in units of kcal/mol. Distances and spin densities for these structures are reported in Table 3. Histidine of the T2 removed for clarity. Colors: Cu, orange; O, red; N, blue; C, gray; H, white. ET/PT, PT/ET, and EPT pathways labeled in red, blue, and black, respectively.

Table 3. Selected Geometric Parameters and Copper Spin Densities of the Structures of the Second IET Step

	$NI^{2e,H}$	$NI^{e,2H}$	$NI^{2e,2H}$ (MV)	$NI^{2e,2H}$ (L)
	Distances (Å)			
T3a–T3b	3.827	4.509	4.558	4.044
T3a–T2	4.022	4.503	4.301	4.127
T3b–T2	3.790	3.724	3.758	4.179
T3b–O(inner)[a]	1.900	2.000	1.960	2.081
T2–O(inner)[a]	2.032	1.924	1.966	2.254
T3a–O(outer)[b]	2.090			2.217
T3b–O(outer)[b]	1.938	1.986	2.200	1.956
T2–OH_2	2.140	1.954	2.061	2.087
Cu Spin Densities				
T3a	0.01	−0.00	0.00	0.04
T3b	0.54	−0.67	0.37	0.59
T2	0.06	0.63	0.32	0.02

[a]O(inner) is μ_2-OH in $NI^{e,2H}$, and $NI^{2e,2H}$ (MV) and H_2O in $NI^{2e,2H}$ (L). [b]O(outer) is μ_2-OH $NI^{2e,2H}$ (L) and H_2O in $NI^{2e,2H}$ (MV) and $NI^{e,2H}$.

elongation of the T3a bond to the μ_2-OH where the oxidized T3b and T2 are antiferromagnetically coupled (NI^{e}). Protonation of the μ_3-oxo of NI^{e} gives $NI^{e,H}$ where the newly generated μ_2-OH bridge provides a superexchange pathway for antiferromagnetic coupling of the oxidized T2 and T3b Cu's with a free energy for EPT [$\Delta G(e^- + H^+)$] of −31.8 kcal/mol and λ_i^{EPT} = 1.1 eV as consistent with previous calculations for this IET step.[23] This large negative free energy is clearly an overestimation that can be attributed to the B3LYP functional, which overestimates the covalency of the T1 site.[8,9,42] This can be corrected for by reference to equivalent calculations of the resting state where the calculation gives −21.3 kcal/mol while the experimental value is given by the electrochemical potential difference between the T1 and T3 sites in the resting enzyme (ΔG = −2.0 kcal/mol).[23,43] Using this "resting" calibration, the experimentally calibrated free energy for EPT for the first IET step in NI reduction is −12.5 kcal/mol.

If NI is first protonated, this protonation can occur at either the μ_3-oxo or μ_2-OH ligands. Protonation of the μ_2-OH results in the breaking of the T3a-μ_2-OH bond leading to a ground state spin change from $S = {}^1/_2$ to $S = {}^3/_2$ [NI^{H}(T3W), where T3W denotes "T3 water"].[2,20] Protonation of the μ_3-oxo gives NI^{H}, which is 18.2 kcal/mol more favorable compared protonation of the μ_2-OH reflecting a ΔpK_a of ∼13 between the μ_3-oxo and μ_2-OH ligands quantifying the strong basicity of the μ_3-oxo (Figure 8). Interestingly, the decay of NI due to protonation of the μ_3-oxo is slow.[22] Since the TNC oxygen

dx.doi.org/10.1021/ja509150j | J. Am. Chem. Soc. 2014, 136, 17788−17801

ligands are protonated by a carboxylate near the T3 edge of the TNC (E487 in Figure 1), protonation of the less basic μ_2-OH would precede protonation of the μ_3-oxo leading to slow rate for NI decay. The protonation of NI will be considered below.

These calculations are consistent with the kinetic findings of rapid first IET and show this process has a large driving force for rapid EPT due to the μ_3-oxo acting as a strong base (diagonal arrow from **NI** to $\mathbf{NI^{e,H}}$ in Figure 8).[23] Additionally, the inner-sphere reorganization energy for the EPT in the first IET process is calculated to be 1.1 eV, which is predominantly due to the loss of the T3a-μ_3-oxo bond upon protonation.

Second IET Step and Correlation to EPR Active Intermediate. Starting from $\mathbf{NI^{e,H}}$, electron transfer to this intermediate results in reduction of the T2 Cu with a computed ET inner-sphere reorganization energy of 0.4 eV ($\mathbf{NI^{2e,H}}$ in Figure 9).Protonation of this intermediate Protonation of this intermediate ($\mathbf{NI^{2e,H}}$) can occur at the μ_2-OH bridging the T2 and T3b Cu's (inner μ_2-OH) or at the T3a and T3b Cu's (outer μ_2-OH). Protonation of the outer μ_2-OH results in a mixed-valent (MV) delocalized intermediate [$\mathbf{NI^{2e,2H}}$ (**MV**)] with the electron shared equivalently between the T2 and T3b Cu's where the bond of the reduced T3a to the μ_2-OH has been cleaved (Cu spin densities in Table 3). Protonation of the inner μ_2-OH yields an intermediate where a water ligand is bound inside the TNC with a localized hole (**L**) on the oxidized T3b giving $\mathbf{NI^{2e,2H}}$ (**L**). Protonation to give $\mathbf{NI^{2e,2H}}$ (**MV**) is calculated to be 6.3 kcal/mol more favorable than protonation to form $\mathbf{NI^{2e,2H}}$ (**L**).

In the PT/ET process (blue arrows Figure 9), protonation of $\mathbf{NI^{e,H}}$ only occurs at the outer μ_2-OH cleaving the reduced T3a μ_2-OH bond to give $\mathbf{NI^{e,2H}}$. Attempts to optimize a protonated inner water ligand (from μ_2-OH) results in proton transfer to the outer μ_2-OH due to a lower pK_a of the μ_2-OH bridging the oxidized T2 and T3b coppers. Reduction of $\mathbf{NI^{e,2H}}$ gives the same $\mathbf{NI^{2e,2H}}$ (**MV**) obtained by first reducing $\mathbf{NI^{e,H}}$ where the ET inner-sphere reorganization energy for this step is 0.4 eV. This MV structure can be further protonated at the inner μ_2-OH to obtain a structure with an oxidized, localized T3b $\mathbf{NI^{2e,3H}}$, which is uphill by 7.2 kcal/mol

From the kinetics analysis above, the second IET step is particularly interesting since it occurs with a low driving force but is required to be rapid to be consistent with turnover. As in the first IET, the computed free energies in this step can calibrated to the experimental driving force for the reduction of the fully oxidized resting state and compared to the $\Delta G(e^- + H^+)$ for EPT.

First, an EPT process (black arrows in Figure 9) for the second IET step is considered. Compared to the $\Delta G(e^- + H^+)$ for first IET step, the computed $\Delta G(e^- + H^+)$'s for EPT to give the $\mathbf{NI^{2e,2H}}$ (**MV**) and (**L**) intermediates are less favorable by ~10 and ~17 kcal/mol, respectively, consistent with the lower driving force for this step compared to the first from the kinetics. The "resting" calibrated EPT free energy to give $\mathbf{NI^{2e,2H}}$ (**MV**) is $\Delta G(e^- + H^+)$ = −2.1 kcal/mol and is also consistent with the experimentally determined low driving force. From Marcus Theory, if the first and second IET steps occur with similar, rapid rates (>700 s^{-1}), the low driving force for this second IET step requires it to occur with a reorganization energy at least 0.8 eV lower than the first IET step.[44] However, due to large geometric changes upon EPT (Figure 9), the computed inner-sphere reorganization energies for EPT for the second step are large and comparable to that of the first [1.2 eV for $\mathbf{NI^{2e,2H}}$ (**MV**) and 0.9 eV for $\mathbf{NI^{2e,2H}}$ (**L**)]. Thus, a concerted process for the second IET step would not be fast or catalytically relevant. The ET/PT mechanism (red arrows in Figure 9) would also be slow as it is calculated to be ~30 kcal/mol less favorable than the first IET. This would require ~2.0 eV lower λ_i than the first IET. However, the λ is calculated to be only 0.8 eV less than the first.

Alternatively, a PT/ET process (blue arrows in Figure 9), where the proton transfer to the outer μ_2-OH precedes ET to give the $\mathbf{NI^{2e,2H}}$ (**MV**) form, has a driving force for ET ~10 kcal/mol less than the first IET step and an ET inner-sphere reorganization energy of 0.4 eV. This difference in driving force would require a 0.8 eV lower reorganization energy for IET to have the same rate (>700 s^{-1}). This is consistent with the difference in computed reorganization energies for EPT (1.1 eV) in the first step and PT/ET in the second (0.4 eV). Therefore, rapid IET for the second IET step would occur after protonation of the outer μ_2-OH of the $\mathbf{NI^{e,H}}$ intermediate.

In order for this IET process to be rapid and stepwise, the proton transfer to the outer μ_2-OH must be fast. Interestingly, the free energy for protonating the outer μ_2-OH of $\mathbf{NI^{e,H}}$ is similar to protonating the μ_3-oxo in NI, 0.2 and −2.9 kcal/mol, respectively, implying that these ligands have similar basicities and would rapidly protonate. However, NI decay, which involves this protonation of the μ_3-oxo, is slow.[22]

Slow protonation of **NI** is due to barriers in the PT process where protons originate from E487 near the μ_2-OH bridge of the T3 Cu's (Figure 1). To determine the differences in the rates of PT to the μ_2-OH of $\mathbf{NI^{e,H}}$ relative to the μ_3-oxo in **NI**, PT mechanisms were computed (Figure 10). In these models, a proton was transferred to the TNC from a carboxylic acid modeling E487.[45] PT to the μ_2-OH of **NI** leads to a transition state (TS; 9.8 kcal/mol) where the T3aCu(II)−μ_2-OH bond is broken due to the incoming proton. Upon cleavage of the T3aCu(II)−μ_2-OH bond, the spin ground state changes from $S = {}^1/_2$ to ${}^3/_2$ [$\mathbf{NI^H(T3W)}$; ΔE = 4.0 kcal/mol].[2,20] Note that the energy of protonation of the μ_2-OH of NI from solvent is computed to be ΔE = 9.1 kcal/mol (ΔG = 15.3 kcal/mol in Figure 8). The ~5 kcal/mol more favorable protonation by the carboxylic acid reflects greater stability due to the stronger hydrogen bond from the anionic carboxylate compared to a neutral water (Figure 8). PT from T3b−OH_2 to the μ_3-oxo leads to another transition state (TS′; 11.0 kcal/mol, modeled in a 2D potential energy surface; see Supporting Information Figure S8) where the T3bCu(II)−μ_3-oxo bond is broken due a steric clash of the water ligand with the T3aCu(II). From here, the proton is transferred to the μ_3-oxo (−7.7 kcal/mol), which is in good agreement with the energy for protonation of the μ_3-oxo of **NI** in Figure 8 (ΔE = −8.6 kcal/mol; ΔG = −2.9 kcal/mol). Therefore, protonation of the basic μ_3-oxo requires overcoming two barriers due to the cleavage of strong Cu(II)−hydroxo and oxo bonds, the highest being ~11.0 kcal/mol, in the range of the experimentally observed activation enthalpy of ~9−14.[22] Alternatively, PT from the carboxylic acid to the μ_2-OH of $\mathbf{NI^{e,H}}$ is calculated to be downhill (−8.6 kcal/mol) and importantly without a barrier (Supporting Information Figure S10) consistent with the relative energy for protonation of the corresponding structure in Figure 9 (ΔE = −10.1 kcal/mol; ΔG = 0.2 kcal/mol), and comparable with the proton affinity for the μ_3-oxo (Figure 10). This is due to the weakened T3aCu(I)-μ_2-OH in $\mathbf{NI^{e,H}}$, which cleaves prior to PT. This contrasts PT to the μ_2-OH in **NI** that involves breaking a strong Cu(II)-μ_2-OH. Therefore, the μ_2-OH in $\mathbf{NI^{e,H}}$ is kinetically accessible and would protonate rapidly whereas the μ_3-oxo in **NI** is just as

dx.doi.org/10.1021/ja509150j | J. Am. Chem. Soc. 2014, 136, 17788−17801

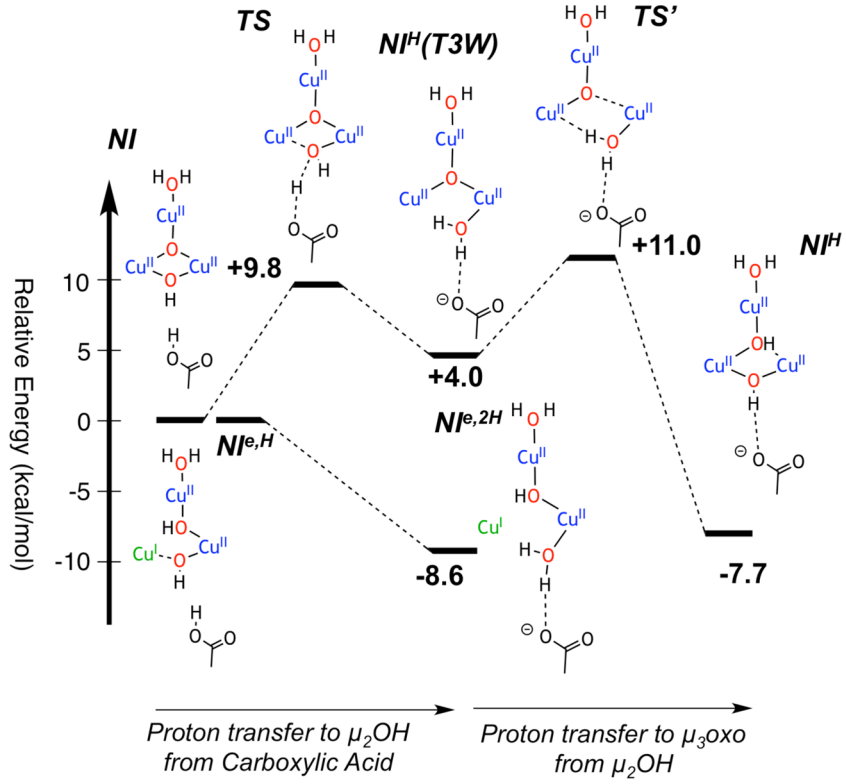

Figure 10. Mechanism of proton transfer from a carboxylate to the μ_2-OH of **NI** and $\mathbf{NI}^{e,H}$ and from the T3b−OH_2 to the μ_3-oxo of NI. Details in Supporting Information.

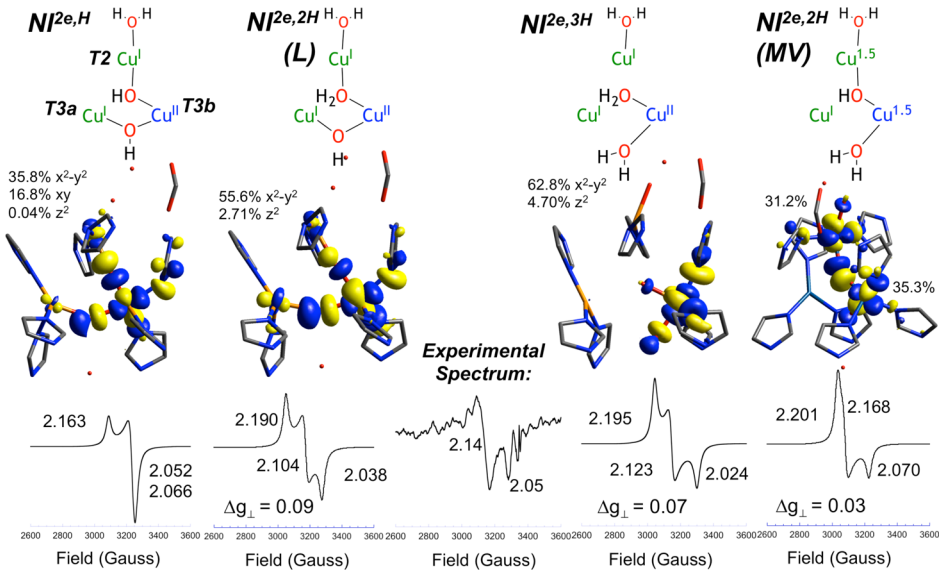

Figure 11. Comparison of the 1-hole intermediates in the reduction of NI. From left to right: $\mathbf{NI}^{2e,H}$, $\mathbf{NI}^{2e,2H}$(**L**), $\mathbf{NI}^{2e,3H}$, and $\mathbf{NI}^{2e,2H}$ (**MV**). (Top) Structures of the intermediates. (Middle) Singly occupied β-LUMOs of the ground state (isodensity value = 0.035). (Bottom) Simulated ESIM X-band from Orca *g*-values (9.35 GHz). The experimental intermediate [T1 subtracted (described as in Supporting Information Figure S3)] X-band EPR spectrum is also included at bottom center.

basic but slow to protonate due to the required breaking of strong Cu(II)−oxo and hydroxo bonds. This would prevent adventitious protonation of NI before it can be reduced (vide infra).

From the above DFT modeling, there are a number of potential EPR active $S = {}^1/_2$ intermediates (Figures 9 and 11). These possible structures for this 1 electron hole intermediate can be correlated to the FQ-EPR data presented in Figure 6 (a derivative feature at $g = 2.14$ and another possible negative contribution at $g = 2.05$).

The $\mathbf{NI}^{2e,H}$ intermediate has a hole localized on the T3b Cu (Figure 11, first structure). In the *g*-tensor coordinate system the ground state is calculated to be $d_{x^2-y^2}$. This predicts an EPR spectrum inconsistent with the experimental signal (Figure 11 bottom center) since this intermediate lacks a derivative feature at low field. The possible $\mathbf{NI}^{2e,2H}$ (**L**) and $\mathbf{NI}^{2e,3H}$ intermediates

dx.doi.org/10.1021/ja509150j | J. Am. Chem. Soc. 2014, 136, 17788−17801

(Figure 11, second and third structures) have localized holes on the T3b Cu also with predominantly $d_{x^2-y^2}$ ground states but with a small amount of d_{z^2} mixing leading to a rhombic splitting of the *g*-values. Therefore, these possible intermediates would exhibit two *g*-values at low field, but only one low field signal is observed experimentally (Figure 11, bottom center). Therefore, these intermediate structures also do not correspond to the FQ-EPR signal.

The fourth potential EPR-active intermediate is **NI^{2e,2H}(MV)**, where the hole is delocalized over the T2 and T3b Cu's, which have $d_{x^2-y^2}$ orbitals with close to equal contributions, but with different orientations (Figure 11 right). The observed *g*-values for a MV system reflect the molecular *g*-tensor that is the vector-coupled product of the local *g*-tensors on each Cu.[46] The *z*-axis of the $d_{x^2-y^2}$ of the T3b is ~90° rotated about the *y*-axis relative to the *z*-axis of the $d_{x^2-y^2}$ of the T2 (Supporting Information Figure S12). This results in a molecular *g*-tensor consisting of two components that are the average of g_x and g_z from the T3b and T2 and a third that is g_y. Consistent with this picture, the predicted *g*-values for **NI^{2e,2H}(MV)** are 2.201 and 2.168, accompanied by a low *g*-value at 2.070. The simulated spectrum (Figure 11, right) from this structure exhibits a derivative signal consisting of two similar *g*-values at low field with another at high field. This is very similar to the one-hole intermediate spectrum [obtained by subtraction of the T1 spectrum from the 1s, Figure 6, spectrum shown at the bottom center of Figure 11 (see Supporting Information Figure S3)]. Therefore, the **NI^{2e,2H}(MV)** predicted EPR spectrum is most consistent with the observed EPR signal that correlates with the 1-hole intermediate observed in the kinetics.

In summary, the experimental findings coupled to these calculations indicate that the TNC carries out a second rapid IET but with a low driving force. A stepwise PT/ET process enables a fast IET rate with a low driving force due to the low inner-sphere reorganization for the ET step. An EPT process would be slow since protonation of the bound oxygen ligands of the TNC results in structural rearrangements that lead to large reorganization energies. The **NI^{e,H}** intermediate is set up to be rapidly protonated because it is located near the carboxylate proton donor and is strongly basic in this partially reduced site. This second IET step provides structural insight into how the TNC of a partially reduced NI is set up to perform rapid IET with a low driving force.

Third IET Step. Starting from the **NI^{2e,2H} (MV)** species (Figure 12), reduction leads to a fully reduced TNC, where the μ_2-OH shifts from bridging the T2 and T3b Cu's to bridging the T3 Cu's with dissociation of the water that was bound to the T3b (**NI^{3e,2H}**). The μ_2-OH bridging the T3 Cu's is accessible to protonation by from E487. Protonation of this μ_2-OH gives the fully reduced TNC where both oxygen atoms from the 4-electron reduction of O_2 are now fully protonated water products. Protonation of **NI^{2e,2H} (MV)** prior to reduction leads to a water bound in the center of the TNC. Compared to the μ_3-oxo of NI or the outer μ_2-OH of **NI^{e,H}** evaluated above, this is ~7−10 kcal/mol less favorable protonation since this water is constrained in the center of the TNC. Reduction of **NI^{2e,3H}** leads to the fully reduced state **NI^{3e,3H} (FR)** where the waters now optimize to outside the TNC.

The kinetic modeling show that the third IET step is rapid and irreversible. The ET/PT pathway (red arrows in Figure 12) for this step lacks sufficient driving force since its uphill from the first EPT step by ~20 kcal/mol [comparing the ET step

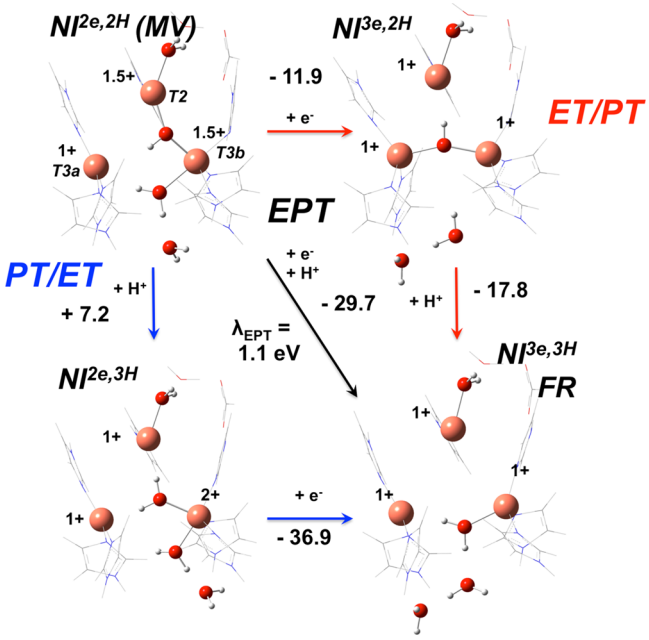

Figure 12. DFT calculations of the third IET step. All energies reflect Gibbs free energies (ΔG) in units of kcal/mol. Distances and spin densities for these structures are reported in Table 4. Histidine of the T2 removed for clarity. Colors: Cu, orange; O, red; N, blue; C, gray; H, white. ET/PT, PT/ET, and EPT pathways labeled in red, blue, and black, respectively.

(−11.9 kcal/mol) to the $\Delta G(e^- + H^+)$ of the first IET]. PT/ET (red arrows in Figure 12) is also unlikely since the proton affinity of **NI^{2e,2H} (MV)** is ~7−10 kcal/mol lower than the protonation of the μ_3-oxo of NI and the μ_2-OH of **NI^{e,H}**, and therefore, this protonation would be slow. However, the free energy for an EPT process [$\Delta G(e^- + H^+) = -10.4$ kcal/mol (calibrated to resting)] is comparable with that of the first IET step, indicating a large driving force for this concerted process that would enable rapid IET even with the large calculated λ_i^{EPT} due to movement of water together with EPT and consistent with experiment.

Although the first and third IET steps have similar driving forces for EPT, they involve different structural changes and therefore have different contributions to the driving force. The

Table 4. Selected Distances and Copper Spin Densities of the Structures of the Third IET Step

	NI^{2e,3H}	NI^{3e,2H}	NI^{3e,3H} (FR)
Distances (Å)			
T3a−T3b	4.703	3.974	4.826
T3a−T2	4.524	4.009	4.561
T3b−T2	4.492	4.193	4.344
T3b−O(inner)[a]	2.086		
T3a−O(outer)[b]		2.061	
T3b−O(outer)[b]	2.055	2.030	2.117
T2−OH_2	2.073	2.192	2.109
Cu Spin Densities			
T3a	0.00		
T3b	0.68		
T2	0.00		

[a]O is H_2O in **NI^{2e,3H}**. [b]O is μ_2-OH in **NI^{3e,2H}** and H_2O in **NI^{2e,3H}** and **NI^{3e,3H}**.

dx.doi.org/10.1021/ja509150j | J. Am. Chem. Soc. 2014, 136, 17788−17801

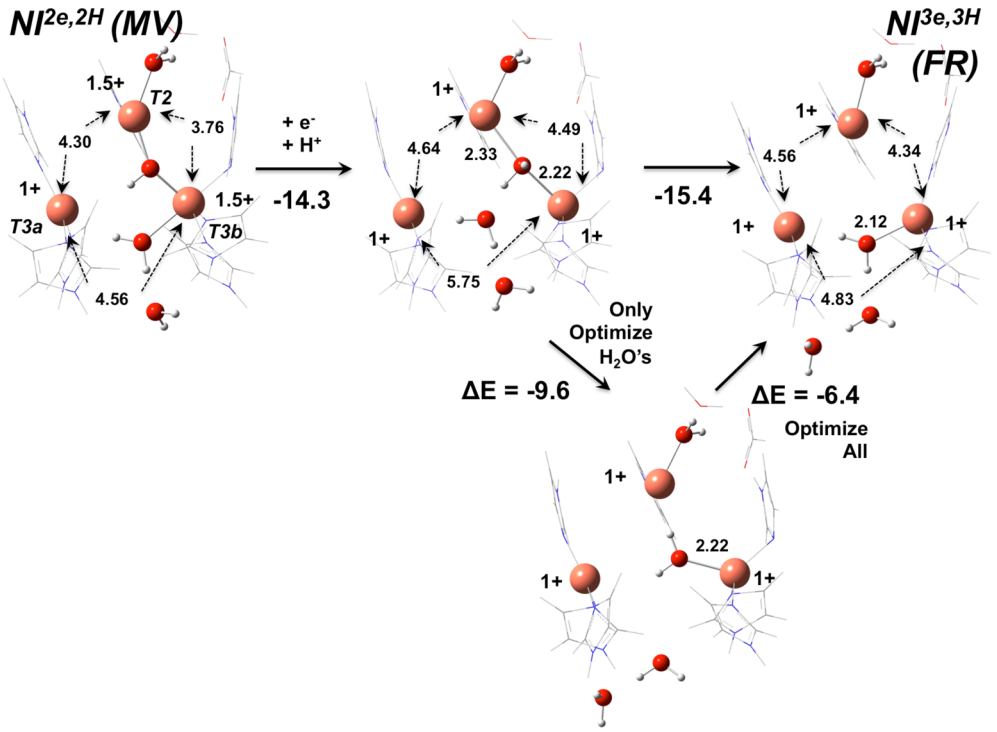

Figure 13. Optimized structures of reduced TNC models emphasizing water extrusion from the fully reduced TNC. Distances in units of Å. Energies in units of kcal/mol. Free energies differences are given for fully optimized structures. Energy differences (ΔE) are given for partially optimized structures. Colors: Cu, orange; O, red; N, blue; C, gray; H, white.

major difference is that the oxygen ligand products of the first IET remain bound to the TNC, while after the third IET the oxygen ligands are fully protonated and optimize out of the cluster. Therefore, loss of water from the fully reduced TNC will contribute to the driving force for EPT.

To estimate the energetic contribution associated with water loss, i.e., water extrusion from within the cluster, a fully reduced TNC structure with waters bound inside the TNC was optimized (Figure 12, middle). Forming this intermediate from $\mathbf{NI}^{\mathbf{2e,2H}}$ (**MV**) has a free energy of $\Delta G(e^- + H^+) = -14.3$ kcal/mol, which represents the driving force for EPT in the absence of water extrusion. Note that upon EPT the μ_2-OH in $\mathbf{NI}^{\mathbf{2e,2H}}$ (**MV**) remains as a water bridge between the T2 and T3b coppers. When the distance of the bridging water to the T2 Cu is elongated from this position, the waters optimize to outside the cluster. The free energy difference to this fully reduced (**FR**) cluster is downhill by −15.4 kcal/mol and is an upper limit on the driving force for water extrusion from the TNC, which is coupled to EPT enabling rapid IET (Figure 12).

The contributions to the driving force are evident from the geometric changes upon water extrusion from the TNC. In the water bound structure (Figure 13, middle), if only the internal waters are optimized (constraining the rest of the cluster), the repulsive interactions of these water ligands with the reduced Cu's are minimized (−9.6 kcal/mol, Figure 13, bottom). Full optimization of the cluster to FR gives shorter Cu−Cu distances reflecting relaxation of the Cu's to their equilibrium positions (−6.4 kcal/mol). The 2.2 Å resolution crystal structure of fully reduced ascorbate oxidase exhibits Cu−Cu distances (T3a−T3b = 5.09 Å, T3a−T2 = 4.03 Å, T3b−T2 = 4.46 Å)[26] consistent with the FR optimized structure (Figure 13, right) and indicate that the Cu−Cu distances in the water bound cluster (Figure 13 right) are indeed long. Thus, waters bound in the center of the cluster undergo steric repulsions with the reduced Cu's and cause these Cu's to distort away from their preferred Cu−Cu distances in the fully reduced cluster. Since the Cu's are held in position by the protein ligands, these protein constraints oppose the waters inside the fully reduced TNC and cause their favorable extrusion in consort with EPT. This water extrusion serves an additional purpose since all three coppers of the reduced TNC need to be coordinatively unsaturated to go on to react with O_2 in catalysis.

DISCUSSION

From a combination of kinetics, EPR spectroscopy, and calculations, the mechanism of the reduction of NI has been evaluated and reveals that the TNC enables three rapid IET processes with three unique structural mechanisms for rapid turnover in catalysis (Figure 14). The first IET step is fast due a large driving force for coupled EPT based on the μ_3-oxo acting as a strong base.[23] From experimental kinetic data, the second IET step has a low driving force that would result in a slow EPT process due to the sizable reorganization energy resulting from large structural changes upon EPT. Instead, a stepwise PT/ET process is effective. The μ_2-OH bridge of the partially reduced TNC is kinetically accessible and basic enough for rapid protonation. This enables rapid ET with a low driving force because of the low inner-sphere reorganization energy. The third IET step completes the reduction of the TNC again through an EPT process, with a large driving force as reduction and protonation are coupled to water extrusion from the fully reduced TNC due to protein constraints from the protein backbone.

A number of attributes enable rapid IET in the turnover of the MCOs. The most important is that reduction of NI requires both three electrons and three protons. This is enabled by the

dx.doi.org/10.1021/ja509150j | J. Am. Chem. Soc. 2014, 136, 17788−17801

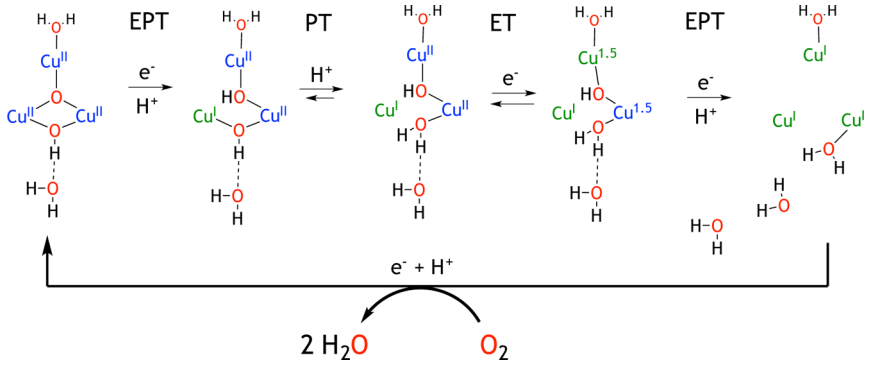

Figure 14. Catalytic mechanism of the MCOs showing each intermediate along the $3e^-/3H^+$ mechanism in the reduction of NI to the fully reduced TNC.

triangular arrangement of the three oxidized coppers of the TNC, which stabilize the reduced oxygen ions, bound as μ_3-oxo and μ_2-OH ligands. Therefore, three electrons and three protons are required to fully reduce the TNC and produce water, which are coupled to enable rapid IET.

The delivery of protons to these ligands at the proper step enables the TNC to protonate the bound oxo and hydroxo ligands with the reduction of the Cu's. This is due in part to the MCOs containing a single entry point for protons (E487) and limited solvent accessibility to prevent adventitious protonation of the basic μ_3-oxo ligand prior to reduction. This is evident from the PT mechanism for NI (Figure 10), where there is a barrier to protonate the basic μ_3-oxo due to the strong Cu(II)–oxo bond in addition to the barrier for protonation of the μ_2-OH. The reduction of the T3a Cu by the first EPT step (to $\mathbf{NI^{e,H}}$) increases the basicity of the T3 μ_2-OH bridge, which is directly accessible from E487 and would rapidly protonate, which enables rapid and reversible ET for the second IET step. Proton delivery in the third step is concerted with ET and coupled to water extrusion.

An essential function of the TNC revealed by this mechanism is making product water binding to the fully reduced TNC unfavorable, which contributes to the driving force for water extrusion. Waters bound inside the fully reduced cluster have steric interactions with the Cu's and distort the reduced Cu's away from their equilibrium positions enforced by the protein. Therefore, the protein constraints on the Cu's of the fully reduced TNC lead to favorable water extrusion, and this contributes to the driving force to enable rapid EPT even with the reorganization energy associated with this structural change. Additionally, coupling water extrusion to the last IET step is critically important in enabling the coordination unsaturation required by the fully reduced TNC for O_2 reduction in turnover.

CONCLUSIONS

The combination of coupling the transfer of electrons to proton delivery and the protein constrains enabling water extrusion reflects a sophisticated mechanistic control by the TNC of the MCOs that enables the three rapid IETs in turnover. All three of these IET steps are rapid because of the basicity of the O_2-derived ligands that arise from cleavage of the O–O bond. In catalysis, the triangular topology of the TNC enables the fast, concerted 4-electron reduction of O_2 to the water level in the formation of NI.[17] However, only after NI is fully reduced by rapid proton coupled IET processes are the water products of O_2 reduction fully protonated and then extruded from the cluster, enabling reduction of another equivalent of O_2. Therefore, the MCOs enable rapid rereduction of the TNC by coupling the three rapid proton-coupled IET processes with the final synthesis of two H_2O molecules from O_2 (Figure 15). This defines a unifying catalytic mechanism by the TNC for coupling O_2 reduction with rapid proton coupled IETs to enable fast turnover in oxidation catalysis.

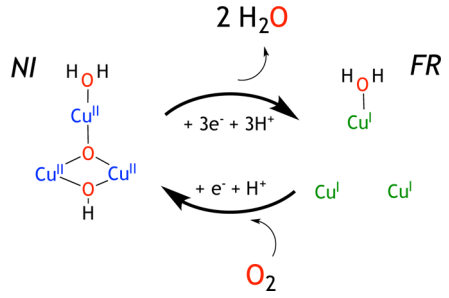

Figure 15. Unifying mechanism of coupling O_2 reduction with rapid IET in the reduction of NI for fast turnover in the catalytic cycle of the MCOs.

METHODS

Experimental Section. All chemicals were reagent grade and used without further purification. Water was purified to a resistivity of 15–17 MΩ cm^{-1} using a Barnstead Nanopure deionizing system. *Rhus vernicifera* laccase was isolated from acetone powder (Saito and Co., Osaka, Japan) according to published procedures.[43,47] Protein concentration was determined using the extinction coefficient of the absorption band at 280 nm (90 000 M^{-1} cm^{-1}).[48] Copper content was determined spectrophotometrically using 2,2′-biquinoline.[49] The concentration of paramagnetic copper was determined from spin quantitation of EPR spectra, using a 1.0 mM $CuSO_4{\cdot}5H_2O$ solution with 2 mM HCl and 2 M $NaClO_4$ standard.[50] Protein samples were buffer-exchanged into 100 mM sodium phosphase buffer (pH = 7.5). Kinetic data with ~2 ms dead time were obtained using an Applied Photophysics SX.20 stopped-flow absorption spectrophotometer equipped with a Hg/Xe Arc lamp and outfitted with PEEK tubing. The temperature was maintained using a water/ethanol temperature bath (Fisher Scientific Isotemp 3016).

Stopped-flow experiments were conducted at 4 °C with a cell path length of 1 cm. All solutions were freshly prepared in an anaerobic glovebox. Protein was deoxygenated under a constant flow of Ar for ~2–3 h and transferred to a glovebox. Both injector ports of the stopped-flow were degassed with ~3.0 mM sodium dithionite for ~20 min and kept anaerobic with nitrogen stream through the system. Concentrations of protein were obtained by measurement of the absorption of the T1 copper at 614 nm (5600 M^{-1} cm^{-1}) of an

dx.doi.org/10.1021/ja509150j | J. Am. Chem. Soc. 2014, 136, 17788–17801

aliquant of anaerobic protein immediately preceding a kinetic experiment. All protein samples were loaded on the stopped-flow at concentrations of 100 μM. To ensure maximal enzyme oxidation while only being single turnover upon reaction with O_2, dioxygen solutions were prepared by diluting air saturated buffer with degassed buffer ~3 fold to produce solution concentrations of $[O_2] \sim 100$ μM.

Kinetics on the native intermediate were conducted by preparing fully reduced protein by adding 4 electron equivalents of excess ascorbate and allowing this to sit for ~30 min to ensure full reduction as also confirmed with color change from blue to colorless. Buffer was added to dilute the reduced enzyme to desired concentration. Native intermediate reduction is measured by addition of excess hydroquinone to the colorless fully reduced protein and dilution to 100 μM concentration followed by reaction with O_2. All kinetic traces of the 365 nm band were fit with Origin 6.0 and KaleidaGraph 4.1 software packages and described previously.[23] Kinetic traces of the 614 nm band were fit with the IBM Chemical Kinetics Simulator version 1.0.1.

All X-band spectra were obtained at 77 K in a liquid nitrogen finger dewar with a Bruker EMX spectrometer, ER 051 QR microwave bridge, and ER 4102ST cavity (parameters for recording the X-band EPR: 9.39 GHz frequency, 10 mW power, and 10 G modulation amplitude). Q-band EPR spectra were obtained at 77 K using an ER 051 QR microwave bridge, an ER 5106QT resonator, and an Oxford continuous-flow CF935 cryostat (parameters for recording the Q-band EPR: 34.0 GHz frequency, 0.44 mW power, and 10 G modulation amplitude). X-band freeze-quench samples were made by reacting reduced laccase (prepared anaerobically in a glovebox) and reacting at 4 °C with equimolar O_2 via syringe directly in the EPR tube with the final enzyme concentration of ~0.2 mM and volume of 100 μL. Q-band freeze-quench samples were made similarly with a final concentration of ~0.5 mM and final volume of ~30 μL. All samples were quenched in acetone−dry ice slurry prior to cooling to 77 K in liquid nitrogen.

Computational. DFT calculations were performed using Gaussian 09 D.01,[51] implementing the spin-unrestricted broken-symmetry method.[52] All geometry optimizations were performed using B3LYP[53] functional with double-ζ basis sets 6-31G* for Cu and coordinated N/O atoms and 3-21G* for the rest. Energies were computed with single points of these optimized structures with TZVP for Cu and coordinated N/O atoms and TZV for the rest.[54] All energies and optimizations were calculated with the polarized continuum model (PCM)[55] as implemented in Gaussian with UAKS atomic radii and a protein dielectric of 4.00.[56] Molecular orbital compositions were determined using the QMForge program.[57] Orbital contours were generated using LUMO.[58] g-tensors were calculated using ORCA with B3LYP and identical TZVP/TZV basis sets as used in the G09 calculations.[59] The starting geometry of the TNC was adapted from the crystal structure of Trametes versicolor laccase[27] (1GYC, Res. 1.9 Å), where the His ligands were replaced by imidazolyl ligands. To reflect the features of the crystal structure, the positions of the H atoms that replaced the side chains to the protein backbone and those bound to His N not bound to Cu (which are all involved in hydrogen bonds) were fixed. All energies were spin purified employing eq 1 for singlet ($S = 0$) and eq 2 for doublet ($S = {}^1/_2$) wave functions where $\langle S^2\rangle_{LS}$ is the computed spin expectation value obtained from the BS wave function.[60,61]

$$ {}^1E = \frac{2^{LS}E - \langle S^2\rangle_{LS}\,{}^3E}{2 - \langle S^2\rangle_{LS}} \quad (1) $$

$$ {}^2E = \frac{3^{LS}E - (\langle S^2\rangle_{LS} - 0.75)^4E}{3.75 - \langle S^2\rangle_{LS}} \quad (2) $$

All optimizations of singly reduced trinuclear models were performed by changing the charge and multiplicity appropriately and obtaining a reduced wave function of the starting structure. A series of single points were carried out by permuting (guess = permute) all relevant copper orbitals to ensure the lowest energy copper was reduced prior to optimization. Free energies of electron transfers were computed using a model of an oxidized and reduced T1 site constructed from 1GYC.[27] Proton transfer energies were modeled by taking into account the solvation free energy of the proton of −260.5 kcal/mol.[36] Inner-sphere reorganization energies for ET steps were computed using an expression depending on the energies of the oxidized (ox) and reduced (red) geometries at the minimum energy structures:[62]

$$ \lambda_i = \frac{1}{2}[E_{ox}(\text{red geom}) - E_{ox}(\text{ox geom}) + E_{red}(\text{ox geom}) - E_{red}(\text{red geom})] $$

Here E_{ox}(red geom) is the energy of the oxidized state in the reduced structure, and E_{red}(ox geom) is the energy of the reduced state in the oxidized structure. Inner-sphere reorganization energies were computed for concerted electron and proton transfer (EPT) processes in a similar manner to that of Hammes-Schiffer and co-workers;[40,41] the energy of the first term in the above expression is obtained by calculating the oxidized energy of the reduced geometry with the transferred proton removed, and the third term was obtained by optimizing a proton on the acceptor oxygen of the oxidized structure and computing the reduced single point energy for this geometry.

■ ASSOCIATED CONTENT

Ⓢ Supporting Information

Figures, tables, and additional text. Complete ref 51. Cartesian coordinates of all models discussed in the text. This material is available free of charge via the Internet at http://pubs.acs.org.

■ AUTHOR INFORMATION

Corresponding Author

edward.solomon@stanford.edu.

Notes

The authors declare no competing financial interest.

■ ACKNOWLEDGMENTS

We thank the National Institutes of Health DK-31450 for funding this research and Dr. Ryan Cowley for helpful discussions.

■ REFERENCES

(1) Solomon, E. I.; Sundaram, U. M.; Machonkin, T. E. *Chem. Rev.* **1996**, *96*, 2563.

(2) Solomon, E. I.; Augustine, A. J.; Yoon, J. *Dalton Trans.* **2008**, 3921.

(3) Solomon, E. I.; Heppner, D. E.; Johnston, E. M.; Ginsbach, J. W.; Cirera, J.; Qayyum, M.; Kieber-Emmons, M. T.; Kjaergaard, C. H.; Hadt, R. G.; Tian, L. *Chem. Rev.* **2014**, *114*, 3659.

(4) Gutteridge, J. M. C.; Stock, J. *Crit. Rev. Clin. Lab. Sci.* **1981**, *14*, 257.

(5) Strong, P. J.; Claus, H. *Crit. Rev. Environ. Sci. Technol.* **2011**, *41*, 373.

(6) Cracknell, J. A.; Vincent, K. A.; Armstrong, F. A. *Chem. Rev.* **2008**, *108*, 2439.

(7) Mano, N.; Kim, H.-H.; Zhang, Y.; Heller, A. *J. Am. Chem. Soc.* **2002**, *124*, 6480.

(8) Solomon, E. I.; Szilagyi, R. K.; DeBeer George, S.; Basumallick, L. *Chem. Rev.* **2004**, *104*, 419.

(9) Solomon, E. I. *Inorg. Chem.* **2006**, *45*, 8012.

(10) Solomon, E. I.; Hadt, R. G. *Coord. Chem. Rev.* **2011**, *255*, 774.

(11) Allendorf, M. D.; Spira, D. J.; Solomon, E. I. *Proc. Natl. Acad. Sci. U.S.A.* **1985**, *82*, 3063.

(12) Spira-Solomon, D. J.; Allendorf, M. D.; Solomon, E. I. *J. Am. Chem. Soc.* **1986**, *108*, 5318.

(13) Quintanar, L.; Yoon, J. J.; Aznar, C. P.; Palmer, A. E.; Andersson, K. K.; Britt, R. D.; Solomon, E. I. *J. Am. Chem. Soc.* **2005**, *127*, 13832.

(14) Taylor, A. B.; Stoj, C. S.; Ziegler, L.; Kosman, D. J.; Hart, P. J. *Proc. Natl. Acad. Sci. U.S.A.* **2005**, *102*, 15459.

(15) Quintanar, L.; Stoj, C.; Wang, T. P.; Kosman, D. J.; Solomon, E. J. *Biochemistry* **2005**, *44*, 6081.
(16) Augustine, A. J.; Quintanar, L.; Stoj, C. S.; Kosman, D. J.; Solomon, E. I. *J. Am. Chem. Soc.* **2007**, *129*, 13118.
(17) Yoon, J.; Solomon, E. I. *J. Am. Chem. Soc.* **2007**, *129*, 13127.
(18) Iwaki, M.; Kataoka, K.; Kajino, T.; Sugiyama, R.; Morishita, H.; Sakurai, T. *FEBS Lett.* **2010**, *584*, 4027.
(19) Cole, J. L.; Ballou, D. P.; Solomon, E. I. *J. Am. Chem. Soc.* **1991**, *113*, 8544.
(20) Yoon, J.; Liboiron, B. D.; Sarangi, R.; Hodgson, K. O.; Hedman, B.; Solomona, E. I. *Proc. Natl. Acad. Sci. U.S.A.* **2007**, *104*, 13609.
(21) Matijošytė, I.; Arends, I. W.; Sheldon, R. A.; de Vries, S. *Inorg. Chim. Acta* **2008**, *361*, 1202.
(22) Huang, H. W.; Zoppellaro, G.; Sakurai, T. *J. Biol. Chem.* **1999**, *274*, 32718.
(23) Heppner, D. E.; Kjaergaard, C. H.; Solomon, E. I. *J. Am. Chem. Soc.* **2013**, *135*, 12212.
(24) Petersen, L. C.; Degn, H. *Biochim. Biophys. Acta, Enzymol.* **1978**, *526*, 85.
(25) Farver, O.; Wherland, S.; Koroleva, O.; Loginov, D. S.; Pecht, I. *FEBS J.* **2011**, *278*, 3463.
(26) Messerschmidt, A.; Rossi, A.; Ladenstein, R.; Huber, R.; Bolognesi, M.; Gatti, G.; Marchesini, A.; Petruzzelli, R.; Finazziagro, A. *J. Mol. Biol.* **1989**, *206*, 513.
(27) Piontek, K.; Antorini, M.; Choinowski, T. *J. Biol. Chem.* **2002**, *277*, 37663.
(28) Gupta, A.; Aartsma, T. J.; Canters, G. W. *J. Am. Chem. Soc.* **2014**, *136*, 2707.
(29) Lee, S. K.; George, S. D.; Antholine, W. E.; Hedman, B.; Hodgson, K. O.; Solomon, E. I. *J. Am. Chem. Soc.* **2002**, *124*, 6180.
(30) Warren, J. J.; Tronic, T. A.; Mayer, J. M. *Chem. Rev.* **2010**, *110*, 6961.
(31) Song, Y.; Buettner, G. R. *Free Radical Biol. Med.* **2010**, *49*, 919.
(32) Roginsky, V. A.; Pisarenko, L. M.; Bors, W.; Michel, C. *J. Chem. Soc., Perkin Trans. 2* **1999**, 871.
(33) Holwerda, R. A.; Gray, H. B. *J. Am. Chem. Soc.* **1974**, *96*, 6008.
(34) Augustine, A. J.; Kragh, M. E.; Sarangi, R.; Fujii, S.; Liboiron, B. D.; Stoj, C. S.; Kosman, D. J.; Hodgson, K. O.; Hedman, B.; Solomon, E. I. *Biochemistry* **2008**, *47*, 2036.
(35) Reinhammar, B. *J. Inorg. Biochem.* **1981**, *15*, 27.
(36) Noyes, R. M. *J. Am. Chem. Soc.* **1962**, *84*, 513.
(37) Marcus, R. A.; Sutin, N. *Biochim. Biophys. Acta* **1985**, *811*, 265.
(38) Layfield, J. P.; Hammes-Schiffer, S. *Chem. Rev.* **2014**, *114*, 3466.
(39) Solis, B. H.; Hammes-Schiffer, S. *Inorg. Chem.* **2014**, *53*, 6427.
(40) Auer, B.; Fernandez, L. E.; Hammes-Schiffer, S. *J. Am. Chem. Soc.* **2011**, *133*, 8282.
(41) Fernandez, L. E.; Horvath, S.; Hammes-Schiffer, S. *J. Phys. Chem. C* **2011**, *116*, 3171.
(42) Hadt, R. G.; Sun, N.; Marshall, N. M.; Hodgson, K. O.; Hedman, B.; Lu, Y.; Solomon, E. I. *J. Am. Chem. Soc.* **2012**, *134*, 16701.
(43) Reinhammar, B. R. M. *Biochim. Biophys. Acta, Bioenerg.* **1972**, *275*, 245.
(44) Using the same difference in driving forces and an H_{DA} in the range 0.1−1.0 cm^{-1}, which is a reasonable estimate for this system, the total reorganization energy must be ∼0.8 eV lower for the second IET step to be as fast as the first.
(45) Crystal structures of the MCOs contain a water between the bridging hydroxide and E487, which is not included in this model. From previous calculations (see ref 17), the presence of this water does not affect the barrier of proton transfer.
(46) Westmoreland, T. D.; Wilcox, D. E.; Baldwin, M. J.; Mims, W. B.; Solomon, E. I. *J. Am. Chem. Soc.* **1989**, *111*, 6106.
(47) Reinhammar, B. *Biochim. Biophys. Acta, Bioenerg.* **1970**, *205*, 35.
(48) Bradford, M. M. *Anal. Biochem.* **1976**, *72*, 248.
(49) Felsenfeld, G. *Arch. Biochem. Biophys.* **1960**, *87*, 247.
(50) Carithers, R. P.; Palmer, G. *J. Biol. Chem.* **1981**, *256*, 7967.
(51) Frisch, M. J.; et al. Gaussian, Inc.: Wallingford, CT, 2009.
(52) Noodleman, L. *J. Chem. Phys.* **1981**, *74*, 5737.
(53) Becke, A. D. *J. Chem. Phys.* **1993**, *98*, 5648.
(54) Schafer, A.; Huber, C.; Ahlrichs, R. *J. Chem. Phys.* **1994**, *100*, 5829.
(55) Miertuš, S.; Scrocco, E.; Tomasi, J. *Chem. Phys.* **1981**, *55*, 117.
(56) Gogonea, V.; Merz, K. M. *J. Phys. Chem. A* **1999**, *103*, 5171.
(57) *QMForge, version 2.3.2*; Adam Tenderholt: 2014.
(58) *Lumo, version 1.0.2*; Matthew Kieber-Emmons: Ephrata, PA, 2014.
(59) Neese, F. *Wiley Interdiscip. Rev.: Comput. Mol. Sci.* **2012**, *2*, 73.
(60) Ziegler, T.; Rauk, A.; Baerends, E. *Theor. Chim. Acta* **1977**, *43*, 261.
(61) Yamaguchi, K.; Jensen, F.; Dorigo, A.; Houk, K. N. *Chem. Phys. Lett.* **1988**, *149*, 537.
(62) Klimkāns, A.; Larsson, S. *Chem. Phys.* **1994**, *189*, 25.